Proceedings of the 20th International Conference on Soil Mechanics and Geotechnical Engineering– Rahman and Jaksa (Eds)

Cavity expansion analysis of pile installation in chalk using synchrotron X-ray computed tomography

Analyse de l'expansion de cavité pour l'installation de pieux dans la craie par tomographie synchrotron aux rayons X

Fernando Alvarez-Borges, Robert Atwood, Thomas Connolley, Nghia Vo & Sharif Ahmed
Diamond Light Source, United Kingdom, fernando.alvarez-borges@diamond.ac.uk

Bangalore Narasimha Madhusudhan & David Richards
Faculty of Engineering and Physical Sciences, University of Southampton, United Kingdom

ABSTRACT: Pile installation in chalk was investigated using physical models and in-situ synchrotron X-ray computed tomography. The aim was to quantify void ratio (*e*) changes in the chalk induced by pile penetration and assess the suitability of drained cavity expansion theory to predict these changes using a critical state model with plastic hardening and cementation degradation. Two experiments were carried out: a cone-tipped pile was slowly and monotonically pushed into the sample to model drained penetration, and an open-ended tube pile was cyclically jacked at a fast rate to mimic partially undrained pile driving. Cavity expansion analysis accurately predicted the remoulded chalk *e* values at the pile wall for both experiments. It also delivered accurate predictions of the radial *e* profiles of the remoulded zone, but accuracy slightly decreased for the partially undrained case. Radial *e* profile predictions for an exhumed field-scale pile from the literature yielded similar results. Analytical results were highly sensitive to the intact chalk density, which affected plastic hardening. The initial stiffness also affected results, but to a lesser degree. The cementation degradation rate had a negligible effect, as cementation strength was found to be small compared to stresses mobilised during plastic hardening.

RÉSUMÉ : L'installation de pieux dans la craie a été étudiée à l'aide de modèles physiques et de la tomographie par rayons X synchrotron in situ. L'objectif était de quantifier les changements du l'indice des vides (*e*) dans la craie induite par la pénétration des pieux et d'évaluer l'adéquation de la théorie de l'expansion de la cavité drainée pour prédire ces changements à l'aide d'un modèle d'état critique avec durcissement plastique et dégradation de la cimentation. Deux expériences ont été réalisées : un pieu à pointe conique a été de façon lente et monotone poussé pour modéliser la pénétration drainée, et un pieu tubulaire à extrémité ouverte a été cycliquement insérée à une vitesse rapide pour imiter le battage de pieux partiellement non drainé. L'analyse de l'expansion de la cavité a prédit avec précision les valeurs du *e* de la craie remoulée dans la paroi du pieu dans les deux expériences. Il a également fourni des prédictions précises des profils radiaux de *e* dans la zone remoulée, mais la précision a légèrement diminué pour le cas partiellement non drainé. Les prédictions du profil radial du *e* d'un pieux exhumée à l'échelle du terrain trouve dans la littérature montré résultats similaires. Les résultats analytiques étaient très sensibles à la densité intacte de craie, qui a affecté le durcissement en plastique. La rigidité initiale a également affecté les résultats, mais dans une moindre mesure. Le taux de dégradation de la cimentation a eu un effet négligeable, car la résistance à la cimentation s'est trouvée faible par rapport aux contraintes mobilisées lors du durcissement plastique.

KEYWORDS: chalk, displacement piles, synchrotron tomography, cavity expansion, physical modelling.

1 INTRODUCTION

Displacement piles supporting offshore infrastructure in the North Sea, Baltic Sea and English Channel are frequently installed in chalk, a soft biomicrite. Chalk crushes during pile installation and forms a remoulded interface, or annulus, around the pile shaft. The characteristics of this interface, like its in-situ density, are believed to affect the unit shaft friction available and, thus, the vertical pile capacity (Hobbs & Atkinson, 1993; Lord et al., 1994). However, there is limited knowledge on the pile penetration mechanisms that produce the remoulded annulus. This limited understanding has led to a design philosophy that may be over-conservative, resulting in potentially substantial unnecessary costs in the deployment of fixed offshore structures, including renewable energy infrastructure such as wind turbines (Jardine et al., 2018).

Recent investigations have used physical models and X-ray computed tomography (XCT) to observe the transition of chalk from the cemented (or 'intact') state to the remoulded condition during pile installation (Alvarez-Borges et al., 2018c; Alvarez-Borges et al., 2021). These works revealed information on pile penetration mechanisms and the remoulded interface, such as the in-situ density and thickness of the latter. Results have also been compared with simplified cavity expansion solutions, which suggested preliminary compatibility with critical state soil mechanics and effective stress-based pile design approaches. However, due to their preliminary nature, these analyses ignored aspects of the mechanical behaviour of chalk, notably the effect of interparticle cementation and strain hardening. Additionally, the experiments concerning these studies were carried out ex-situ (i.e., without simultaneous installation and XCT imaging) and using laboratory X-ray sources. The former increased the risk of sample disturbance, while the latter resulted in image artefacts associated with the limited flux and polychromatic nature of X-ray beams produced by laboratory scanners.

The aim of the present paper is to assess the suitability of a novel drained cavity expansion analysis for pile penetration in intact chalk to predict the chalk annulus density profile. This analysis retains the simplicity of previous approaches while incorporating plastic hardening and cementation degradation effects. To carry out this investigation, a new set of model pile installation experiments using in-situ synchrotron XCT imaging were performed. This technique delivers image resolution levels that cannot been achieved by laboratory based XCT scanners for experiments at this scale, while also minimising image artefacts associated with polychromatic X-ray sources.

2 EXPERIMENTAL METHODOLOGY

2.1 *Sample preparation*

Chalk block samples were collected from a quarry near St Nicholas-at-Wade (SNW), in Southeast England. This sampling site is described in detail by, e.g., Buckley et al. (2018a). Samples were obtained from the Seaford Chalk Formation and exhibited a mean bulk density of 1.97 Mg/m^3 (mean intact dry density of 1.54 Mg/m^3). A chalk block was saturated in chalk-infused de-aired water and sculpted into two 100 mm diameter by 112 mm high cylinders using a soil lathe. Each sample was placed inside a 5 mm-thick polymethyl methacrylate (PMMA) tube and the clearance between the chalk sample and the tube was filled using a high-strength epoxy resin, as described by Alvarez-Borges et al. (2021).

2.2 *Pile installation*

Two aluminium model piles were used: a 60° cone-tipped pile of 6.40 mm in diameter (Exp. 1) and an open-ended tube pile of 7.90 mm in outside diameter and 0.90 mm wall thickness (Exp. 2), both of 65 mm in length. The piles were installed in the chalk specimens using an Instron 8800 series servohydraulic test frame fixed to the tomography stage. The cone-tipped pile was installed at a monotonic rate of 0.100 mm/min which aimed to achieve fully drained penetration. This installation rate is about 2000 times slower than the 1200 mm/min penetration rate used in the 36 mm cone penetration test (CPT) after accounting for the difference in size. The pile geometry also intended to mimic the CPT probe. The tube pile was installed using a pseudo-dynamic method inspired by Lehane & White (2005). The piles were installed in a series of 1 mm embedment depth increments each followed by 0.20 mm extraction, at approximately 10 mm/min. This rate aimed at achieving partially undrained penetration.

Installation was carried out in five steps. The first step drove the pile tip to an initial depth of 20 mm, while subsequent steps increased the embedment depth by 5 mm each until reaching a final pile tip depth of 40 mm.

It is important to note that the sample to pile diameter ratio used was a compromise between a large ratio that minimises boundary effects and the capabilities of the imaging system, as noted by Alvarez-Borges et al. (2021). Circumferential strains measured on the outside surface of the PMMA confinement by these authors in similar experiments suggest that boundary effects may persist with the experiment geometry used.

2.3 *XCT scanning and image reconstruction*

XCT scans were performed using beamline I12 at Diamond Light Source. A 145 keV monochromatic X-ray beam was used with the large field of view X-ray camera described by Drakopoulos et al. (2015). The size of the field of view (FOV) for each scan was 87 mm wide by 19 mm high, approximately, with a pixel size of 0.0215 mm. A series of five vertically overlapping (or 'rastered') scans were performed to cover the entire pile embedment depth and the zone below the pile tip. Limited angle tomography acquisition was needed to prevent the pillars of the Instron frame from blocking the X-ray beam. Thus, 2689 projections were acquired within a 134.4° angular range. The exposure time was one second.

Tomographic reconstruction was carried out using Savu 3.0 (Ramachandran & Lakshminarayanan, 1971; Paganin et al., 2002; Atwood et al., 2015; van Aarle et al., 2016; Wadeson & Basham, 2016; Vo et al., 2018). Reconstructed volumes from the rastered scans were assembled using horizontal tomography slice registration and tapered overlaps, to be able to visualise the entire sample, as presented in Figure 1.

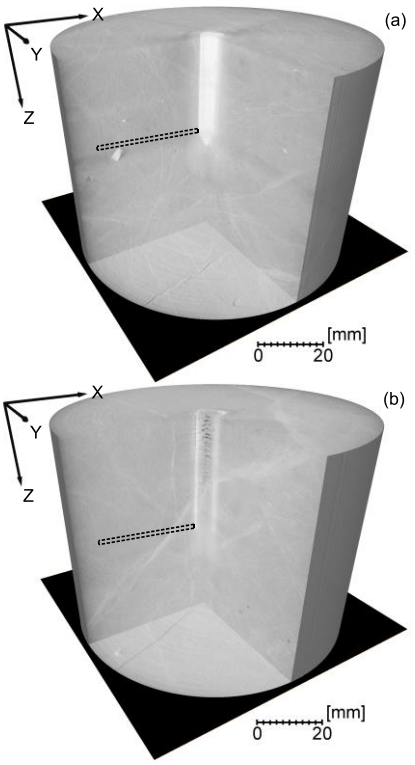

Figure 1. Reconstructed and assembled post-installation raster scans: (a) Exp 1; (b) Exp 2. Pile shown at volume centre; example GV sampling regions marked by dotted boxes; XY slice shown at lower end.

2.4 *Void ratio measurements*

Average radial (or horizontal) grey value (GV) profiles of the chalk sample starting at the cone or pile tip shoulder were produced from vertical (XZ) slices of the reconstructed scans. Sampling locations are schematically shown in Figure 1. GVs from XCT images obtained using monochromatic X-rays are approximately linearly correlated with bulk density in materials of homogeneous mean atomic number. Therefore, bulk density estimates may be derived from GVs by way of a calibration function. Such a calibration function, shown in Figure 2, was derived using the mean GV and the measured bulk densities of the aluminium pile, the 'far-field' intact chalk, the epoxy resin and air. The function was then used to convert GV profiles into bulk density profiles, and these in turn were transformed in to void ratios (e) by assuming full-saturation and using the equation (after Madhusudhan & Baudet (2014)):

$$e = \frac{(G_s\rho_w - \rho_c)}{(\rho_c - \rho_w)} \quad (1)$$

Where G_s is the specific gravity of chalk (taken as 2.70, after Clayton (1983)), and ρ_w and ρ_c are the bulk densities of water and intact chalk, respectively.

3 CAVITY EXPANSION ANALYSIS

3.1 *Definition*

Cavity expansion theory proposes that pile penetration resembles the growth of a spherical or cylindrical cavity in a continuous isotropic elastoplastic medium. The analysis is regularly carried out assuming symmetry around the vertical (Z) axis and plane strain conditions in the direction of cavity growth. In the present analysis, only cylindrical expansion is considered. It is also assumed that expansion occurs in fully drained conditions and that all stresses are effective stresses.

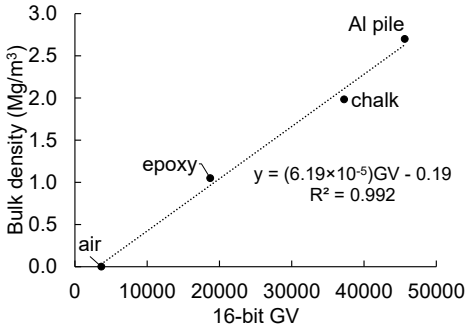

Figure 2. Bulk density-GV calibration.

Before expansion, the cavity is assumed to have a radius a_0 while the geomaterial around it is subject to a radial stress of P_0. As the cavity grows from a_0 to a (i.e., the pile radius), the radial stress around the cavity increases from P_0 to σ_r, and any material point at a radial position r around the cavity is displaced by a distance u. However, displacements are assumed to be recoverable beyond a radius $r = b$, termed the 'elastic-plastic' boundary. As r increases beyond b, $u \to 0$ and $\sigma_r \to P_0$.

The stress equilibrium condition around the expanded cavity is defined as (Carter et al., 1986):

$$\sigma_r - \sigma_\theta + \frac{d\sigma_r}{dr} r = 0 \tag{2}$$

Where σ_θ is the circumferential (or hoop) stress and $d\sigma_r/dr$ represents the change in σ_r with the change in distance from the cavity axis of symmetry (centreline). σ_r and σ_θ are the major and minor principal stresses, respectively.

A Mohr-Coulomb yield criterion for cohesive-frictional geomaterials is adopted (Carter et al., 1986):

$$\sigma_r = \frac{2c\cos\phi}{1-\sin\phi} + \frac{1+\sin\phi}{1-\sin\phi}\sigma_\theta \tag{3}$$

Where ϕ is the mobilised angle of friction and c is the mobilised cohesion, defined as (Schnaid & Mántaras (2003)):

$$c = \frac{c_0}{(1+\gamma-\gamma_p)^n} \tag{4}$$

Where c_0 is the intact cohesion intercept, γ_p is the shear strain at yield, γ is the current shear strain, and n is a cementation degradation factor.

The flow rule by Rowe (1962) is used to define stress-dilatancy:

$$D = -\frac{\delta\varepsilon_V^p}{\delta\varepsilon_r^p} = \frac{\sigma_r/\sigma_\theta}{\tan^2\left[45+\left(\frac{\phi_c}{2}\right)\right]+\left(\frac{2c}{\sigma_\theta}\right)\tan\left[45+\left(\frac{\phi_c}{2}\right)\right]} - 1 \tag{5}$$

Where ϕ_c is the critical state angle of friction (in °) and $\delta\varepsilon_V^p/\delta\varepsilon_r^p$ is the rate of plastic volumetric strain increment. In turn, state-dilatancy is defined following Been & Jefferies (1985) and Bolton (1986):

$$0.8\psi = \phi - \phi_c = A[\exp(-\xi) - 1] \tag{6}$$

Where ψ is the mobilised dilation angle, A is a material constant and ξ is the state parameter, defined as the difference between the current void ratio and the void ratio at the critical state line (CSL), e_c. The latter is obtained using the CSL proposed by Alvarez-Borges et al. (2020) expressed in terms of principal stress invariant $s' = (\sigma_r + \sigma_\theta)/2$:

$$e_c = 0.895 - 0.068(s'/s_{ref})^{0.186} \tag{7}$$

Where the units of s' are kPa and $s'_{ref} = 1$ kPa for consistency.

3.2 *Solution strategy*

The solution strategy is based on the method proposed by Cook (2010) and Hao et al. (2010). It consists in discretising the plastic zone in a series of thin shells and solving stresses and strains at each shell boundary, starting from the elastic-plastic boundary, and progressing inwards until reaching the cavity wall. Logarithmic strains are adopted to handle large deformations, and are defined as:

$$\varepsilon_r = -\ln\left(\frac{dr}{dr_0}\right) = -\ln\left(\frac{r_j - r_i}{(r_j-u_j)-(r_i-u_i)}\right) \tag{8}$$

$$\varepsilon_\theta = -\ln\left(\frac{r}{r_0}\right) = -\ln\left(\frac{r_i}{r_i-u_i}\right) \tag{9}$$

$$\varepsilon_v = -\ln\left(\frac{V}{V_0}\right) = -\ln\left(\frac{r_j^2 - r_i^2}{(r_j-u_j)^2-(r_i-u_i)^2}\right) \tag{10}$$

Where ε_r, ε_θ and ε_v are the radial, circumferential, and volumetric strains, in each case. Shear strains are taken as $\gamma = \varepsilon_r - \varepsilon_\theta$. Subindexes i,j refer to the inner and outer boundaries of the shell, respectively. V_0 and V are the shell volume before and after expansion. Subindex 0 refers to conditions before cavity growth, as before. Elastic deformations are assumed to be negligible within the plastic zone.

The solution proceeds as follows:

1. An initial arbitrary size for the plastic zone radius b is chosen and divided into an m number of shells, so that all shells share identical dr thickness.
2. P_0 is derived from, e.g., the embedment depth, effective unit weight and horizontal-to-vertical effective stress ratio. To retain stress equilibrium beyond the elastic-plastic boundary (Eq. 2), it is assumed that $2P_0 = (\sigma_r + \sigma_\theta)$ when $r = b$.
3. The radial displacement at b, u_b, is calculated by considering that σ_r at b equals the compressive yield stress, P_y. By using the yield shear modulus G_0 and the peak angle of friction ϕ_p, it follows from Eq. 3 that:

$$u_b = \varepsilon_{r=b} b = \frac{P_y - P_0}{2G} b$$
$$u_b = \left(\frac{b}{2G_0}\right)\left[c_0\cos\phi_p + P_0(1+\sin\phi_p)\right] \tag{11}$$

4. It is then considered that $\varepsilon_\theta = -\varepsilon_r$, $\varepsilon_v = \varepsilon_r + \varepsilon_\theta$ and the remaining parameters at b are derived using Eqs. 4-7.
5. Computation proceeds to the inner boundary i of the outer shell with $j = b$. ϕ and c are updated using Eqs. 4 and 6 by assuming that the value of ψ and γ calculated at j applies at i, which is reasonable for very thin shells. σ_r is obtained by considering that $N = (1 + \sin\phi)/(1 - \sin\phi)$ and combining the yield criterion (Eq. 3) with the equilibrium condition (Eq. 2) and integrating, which leads to (Carter et al., 1986):

$$\sigma_{ri} + c\cot\phi = (\sigma_{rj} + c\cot\phi)\left(\frac{r_j}{r_i}\right)^{(N-1)/N} \tag{12}$$

6. The displacement u at i is calculated by invoking the flow rule (Eq. 5) and numerically solving the following (Cook, 2010; Hao et al., 2010):

$$\varepsilon_{vj} + D\gamma_j = \ln\left\{\frac{\left[\frac{(r_j-u_j)^2-(r_i-u_i)^2}{r_j^2-r_i^2}\right]\left[1+\frac{u_i-u_j}{r_j-r_i}\right]^D}{\left[1-\frac{u_i}{r_i}\right]^D}\right\} \tag{13}$$

7. The remaining parameters, including the updated values for ψ, c and γ to be used in the computations for the next shell, can be derived via Eqs. 4-10.
8. The procedure (steps 5-7) is repeated for the subsequent shells. A solution is found when $r_i = u_i = a$ (in practice, a should be reduced by a small amount as Eq. 13 yields a singularity at $u_i = r_i$). If a solution is not reached, then b needs to be adjusted and the procedure repeated from step 1. Iterations may be implemented within a root-finding algorithm by considering that the output r_i and u_i for the last shell are a function of b.

3.3 *Parameter derivation*

The geomaterial parameters required in the cavity expansion solution presented above are c_0, ϕ_c, ϕ_p, G_0, A and n.

Buckley et al. (2018a) report that c_0 = 387 kPa from triaxial tests on intact samples collected at the SNW site. A ϕ_c value of 33.7° was reported by Alvarez-Borges et al. (2020) from undrained triaxial tests on remoulded SNW chalk. Similarly, Buckley et al. (2018a) measured a ϕ_p value of 41° for intact chalk in drained triaxial tests. Buckley et al. (2018a) also measured G_0 values for the Chalk mass (via seismic CPTs) ranging from 0.25 to 1.20 GPa. However, the stiffness of intact chalk is significantly higher than that of the formation. Matthews & Clayton (1993) reported an initial Young's modulus for intact chalk of similar intact dry density of about 9 GPa, which suggests a G_0 value of about 3.6 GPa for the SNW samples if a Poisson ratio of 0.25 is adopted (after Lord et al. (2002)).

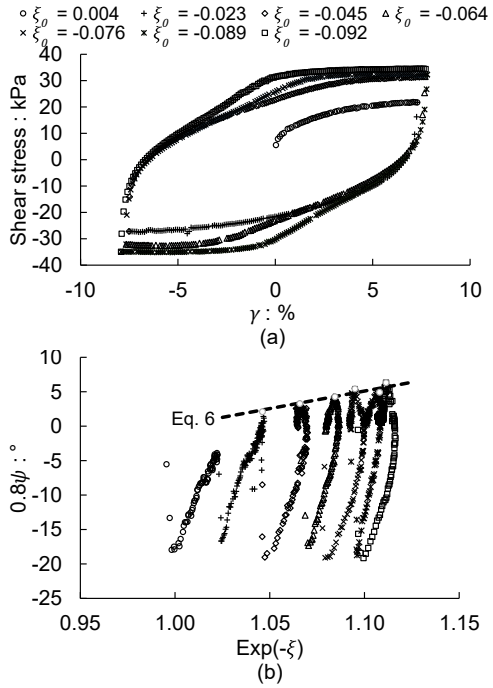

Figure 3. Multistage drained monotonic simple shear test results (a) and derivation of state-dilatancy Eq. 6. ξ_0 refers to the state parameter at the start of each shearing stage.

The dilatancy parameter A (= 51) was obtained from a multistage direct simple shear test on destructured SNW chalk, shown in Figure 3. Samples were prepared using a slurry reconstitution method to capture a wide ξ range. Tests were carried out in drained conditions at a constant vertical stress of 50 kPa. Eq. 6 was fitted to peak dilatancy values derived from the test, as shown in Figure 3b. Further test set-up details are available in Alvarez-Borges et al. (2018a).

Detailed drained triaxial test data for intact SNW chalk from which the cementation degradation parameter n may be estimated are not readily available in the literature. Different values were assessed and are discussed later.

4 RESULTS AND DISCUSSION

Figure 4 compares the radial e profiles extracted from the reconstructed XCT scans and those resulting from the cavity expansion analysis. In the case of Exp. 2, the analysis has been carried out using the equivalent radius $R^* = [(R_o)^2 - (R_i)^2]^{0.5}$, where R_o and R_i are the inside and outside pile radii (after Jardine & Chow (1996)). m and a_0 were 4000 and 0, respectively.

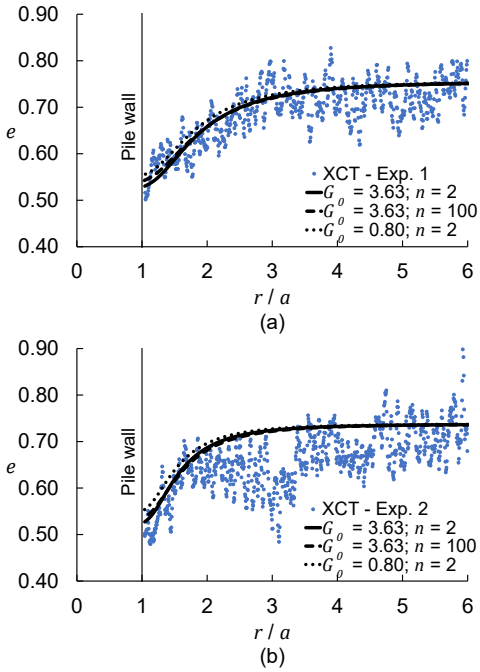

Figure 4. Radial void ratio profiles from XCT measurements and cavity expansion analysis: (a) Exp. 1; (b) Exp. 2. G_0 units are GPa; radial distance r is normalised by the pile radius a.

A relatively good correlation between the analytical solution and the measured data can be achieved for both experiments, though the correlation is stronger for Exp. 1 featuring the cone-tipped model pile (Figure 4a). The somewhat poorer correspondence between predicted and measured e profiles for Exp. 2 (Figure 4b) could originate from the pile installation procedure. The pseudo-dynamic pile installation method used involved much faster penetration rates than in Exp. 1, and it is presumed to have led to partially undrained penetration. The restriction of plastic volumetric strains associated with this may have required the displacement and damage of a proportionally larger volume of chalk to be able to lodge the pile, despite small immediate e reductions. Then, e values throughout the damaged zone could be expected to have reduced as penetration ended and pore pressures dissipated. Fast post-installation pore pressure dissipation has been reported in field-scale instrumented pile tests at SNW by Buckley et al. (2018a), which supports the above observations. Furthermore, Buckley et al. (2018b) carried out a set of field tests using open-ended driven piles (R_0 = 139 mm; R_i = 130.50 mm), some of which they exhumed after installation to measure radial water content profiles from which e values may be derived (by assuming full saturation). The average e profile from these field tests is compared with cavity expansion predictions in Figure 5, which depicts a broadly similar trend to that of Exp. 2 shown in Figure 4b.

Figure 4 shows that adopting a low or high value for the cementation degradation parameter n appears to have little effect

on the predicted e profiles. This is proposed to reflect the structure degradation behaviour of intact chalk. Previous studies have shown that a post-yield structure-permitted space for intact chalk, as defined by Leroueil & Vaughan (1990), is found above the remoulded normal compression line (NCL; Alvarez-Borges et al. (2018b)). The structure-permitted space is bounded by a family of metastable yield surfaces whose size is controlled by the remaining interparticle cementation and by geomaterial fabric (Coop, 1990; Cuccovillo & Coop, 1999). The size of the current yield surface reduces to that of the remoulded material (i.e., chalk without remnants of its original intact structure) once it has undergone significant plastic straining. The role of the remaining interparticle cementation in defining the size of the current yield surface during deformation may be examined by comparing the ratio of the mobilised σ_r and c to the major principal effective stress on the NCL at current void ratio (σ_e). The ratios c/σ_e and σ_r/σ_e are measures of the contribution of cementation to the size of the current yield surface, and of the total size of the yield surface, respectively. This comparison, shown in Figure 6 for Exp. 1, suggests that even when low degradation rates such as $n = 2$ are considered, the contribution of c to the size of the current yield surface during destructuration is modest, as deduced from the separation of both σ_r/σ_e and c/σ_e curves. This indicates that a significant proportion of the mobilised stresses are borne by the destructuring and hardening chalk matrix, rather than the remaining interparticle bonds.

Also observable in Figure 4 is that using a lower value for G_0 for the mass shear modulus of the Chalk formation (in this case the median value reported by Buckley et al. (2018a)) returns in a marginally poorer fit to the XCT data than when using the G_0 value for intact chalk. This is associated with plastic volumetric deformations accumulating at a faster rate as r values move from the elastic-plastic boundary to the cavity wall, resulting in lower e reductions close to the pile. This interpretation suggests that volumetric strains may concentrate close to the pile wall for Chalk Formations exhibiting large horizontal stiffness, thus affecting the thickness and density of the remoulded annulus. However, a comparison of the effect of assuming a 5% higher or lower initial bulk density on predicted e and s' values, shown in Figure 7, evidences that the intact density may have a far greater impact on the deformation pattern arising from pile penetration than G_0. This is attributed in part to the preponderant role of plastic hardening, directly linked to the initial density through the state parameter ξ, in the mobilisation of stresses during cavity expansion, as exemplified in Figure 7.

It is noteworthy that, in both Figure 4 and Figure 5, there appears to be only modest differences amongst measured or predicted e values at the pile wall across both experiments and in the independent field test data. This could also be explained by the prominent role of intact chalk density on the annulus e value at the pile wall, considering that the samples pertaining to this study were obtained from the same site where the field-scale tests were carried out. It could be conjectured that pile wall e values are more directly related to Chalk density than to pile geometry or the installation method. It is therefore tempting to link this correlation between intact chalk and remoulded annulus densities with pile uplift capacity, as implicitly assumed by current CIRIA C574 guidelines (Lord et al., 2002), considering the significant role that the annulus density may have on the available unit shaft friction (Alvarez-Borges et al., 2018a). However, long-term ultimate unit shaft capacities for test piles at the SNW site have ranged from 20 to 168 kPa, with driven piles mobilising much larger capacities than jacked piles, possibly due to the set-up effect (Ciavaglia et al., 2017; Buckley et al., 2018a; Buckley et al., 2018b). It is also unclear if unit shaft friction is linked to e values at the pile wall, or to other e values along the remoulded zone. Thus, the specific mechanisms responsible for these varied results remain elusive. However, the good correlation between predicted and measured e values at the pile wall and throughout most of the remoulded zone suggests that the critical state model for chalk used in the cavity expansion analysis may be suitable, with some modifications, to model other aspects of pile-Chalk interaction such as shaft friction mobilisation.

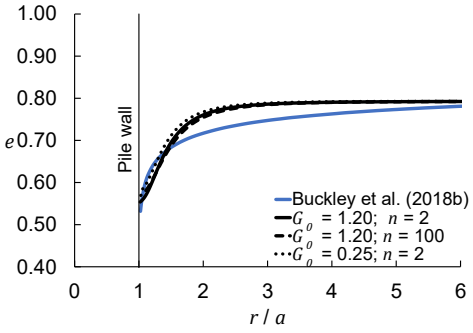

Figure 5. Predicted and measured radial e profiles for field-scale tests.

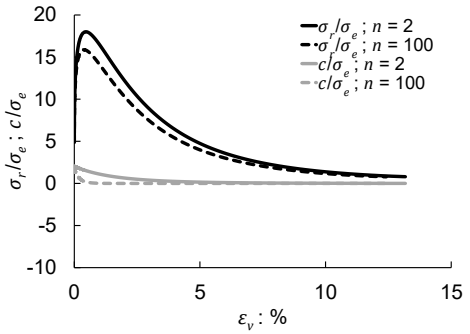

Figure 6. Ratios of σ_r or c to the major principal stress on the NCL, σ_e.

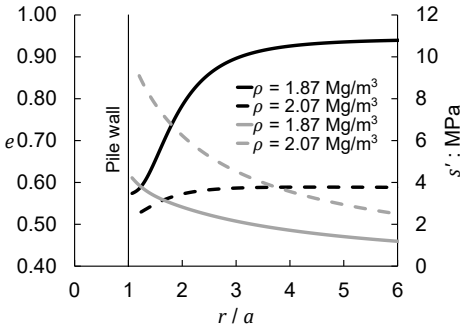

Figure 7. Predicted e and s' profiles using initial bulk densities (ρ) 5% above and below than the 1.97 Mg/m^3 average for the test samples. All other parameters correspond to Exp. 1, using $G_0 = 1.20$ GPa and $n = 2$.

5 CONCLUSIONS

A cavity expansion analysis for pile penetration in intact chalk incorporating cementation degradation and state parameter-based plastic hardening was carried out and compared with the results of scaled physical model experiments with in-situ synchrotron XCT imaging. The objective of the study was to assess whether a cavity expansion solution could adequately model the in-situ void ratio profile of the remoulded chalk annulus that forms during pile installation. Main outcomes of this investigation where:

- The structure degradation factor incorporated into the analysis had a negligible effect on the resulting void ratio profiles. This was due to the proportionally small contribution of cementation to the mobilised stresses.
- Chalk stiffness had a minor effect on predicted void ratio profiles, with lower stiffness values yielding

lower pile wall void ratios due to the wider distribution of volumetric strains throughout the plastic zone.

- Radial void ratio profiles were highly sensitive to the initial density, which heavily influenced plastic hardening through the state parameter.
- Little variability between measured and predicted void ratios at the pile wall was found between experiments and field test data. Considering the predominant role of intact density according to the cavity expansion results, this suggested that other factors like pile geometry and installation method may have a lesser role in defining this value. This did not explain the variability in uplift capacities recorded in pile tests.
- The chalk model used in the cavity expansion method used adequately predicted the radial density profile of most of the remoulded annulus in the experiments. A similar chalk model could be implemented in the future to model shaft friction mobilisation.

6 ACKNOWLEDGEMENTS

The authors acknowledge Diamond Light Source for the provision of beamtime (proposal MG26232-2) and are grateful for the support provided by beamline I12-JEEP staff. The authors also acknowledge the Diamond Light Source-University of Southampton collaboration agreement which provided access to the UKCRIC National Infrastructure Laboratory.

7 REFERENCES

Alvarez-Borges F., Ahmed S., Madhusudhan B.N. & Richards D. (2021) Investigation of pile penetration in calcareous soft rock using X-ray computed tomography. *Int J Phys Model Geo,* Ahead of Print. 10.1680/jphmg.20.00031

Alvarez-Borges F.J., Clayton C.R.I., Richards D.J. & Madhusudhan B.N. (2018a) The effect of the remoulded void ratio on unit shaft friction in small-displacement piles in chalk. *Engineering in Chalk, Proc Chalk 2018 Conf*, pp. 475-480. ICE Publishing. 10.1680/eiccf.64072.475

Alvarez-Borges F.J., Madhusudhan B.N. & Richards D.J. (2018b) The 1D normal compression line and structure permitted space of low-medium density chalk. *Geotech Lett,* 8 (4), 298-304. 10.1680/jgele.18.00091

Alvarez-Borges F.J., Madhusudhan B.N. & Richards D.J. (2020) Mechanical behaviour of low–medium density destructured White Chalk. *Geotech Lett,* 10 (2), 360-366. 10.1680/jgele.20.00009

Alvarez-Borges F.J., Richards D.J., Clayton C.R.I. & Ahmed S.I. (2018c) Application of X-ray computed tomography to investigate pile penetration mechanisms in chalk. *Engineering in Chalk, Proc Chalk 2018 Conf*, pp. 565-570. ICE Publishing. 10.1680/eiccf.64072.565

Atwood R.C., Bodey A.J., Price S.W.T., Basham M. & Drakopoulos M. (2015) A high-throughput system for high-quality tomographic reconstruction of large datasets at Diamond Light Source. *Philos Trans R Soc A,* 373 (2043), 2369–2393. 10.1098/rsta.2014.0398

Been K. & Jefferies M.G. (1985) A State Parameter for Sands. *Géotechnique,* 35 (2), 99-112. 10.1680/geot.1985.35.2.99

Bolton M.D. (1986) The strength and dilatancy of sands. *Géotechnique,* 36 (1), 65-78. 10.1680/geot.1986.36.1.65

Buckley R.M., Jardine R.J., Kontoe S. & Lehane B.M. (2018a) Effective stress regime around a jacked steel pile during installation ageing and load testing in chalk. *Can Geotech J,* 55 (11), 1577-1591. 10.1139/cgj-2017-0145

Buckley R.M., Jardine R.J., Kontoe S., Parker D. & Schroeder F.C. (2018b) Ageing and cyclic behaviour of axially loaded piles driven in chalk. *Géotechnique,* 68 (2), 146-161. 10.1680/jgeot.17.P.012

Carter J.P., Booker J.R. & Yeung S.K. (1986) Cavity expansion in cohesive frictional soils. *Géotechnique,* 36 (3), 349-358. 10.1680/geot.1986.36.3.349

Ciavaglia F., Carey J. & Diambra A. (2017) Time-dependent uplift capacity of driven piles in low to medium density chalk. *Geotech Lett,* 7 (1), 90-96. 10.1680/jgele.16.00162

Clayton C.R.I. (1983) The Influence of Diagenesis on Some Index Properties of Chalk in England. *Géotechnique,* 33 (3), 225-241. 10.1680/geot.1983.33.3.225

Cook B.R. (2010) *Numerical Solution of Cylindrical Cavity Expansion in Sands: Effects of Failure Criteria and Flow Rules.* (MSc Thesis). Pullman, WA, USA: Washington State University.

Coop M.R. (1990) The mechanics of uncemented carbonate sands. *Géotechnique,* 40 (4), 607-626. 10.1680/geot.1990.40.4.607

Cuccovillo T. & Coop M.R. (1999) On the mechanics of structured sands. *Géotechnique,* 49 (6), 741-760. 10.1680/geot.1999.49.6.741

Drakopoulos M., Connolley T., Reinhard C., Atwood R., Magdysyuk O., Vo N., et al. (2015) I12: the Joint Engineering, Environment and Processing (JEEP) beamline at Diamond Light Source. *J Synchrotron Radiat,* 22 (3), 828-838. 10.1107/S1600577515003513

Hao D., Luan M., Li B. & Chen R. (2010) Numerical analysis of cylindrical cavity expansion in sand considering particle crushing and intermediate principal stress. *Trans Tianjin Univ,* 16 (1), 68-74. 10.1007/s12209-010-0013-6

Hobbs N.B. & Atkinson M.S. (1993) Compression and tension tests on an open ended tube pile in chalk. *Ground Engineering,* 26 (3), 30-34.

Jardine R.J. & Chow F.C. (1996) *New Design Methods for Offshore Piles*, London (UK): The Marine Technology Directorate Ltd.

Jardine R.J., Buckley R.M., Kontoe S., Barbosa P. & Schroeder F.C. (2018) Behaviour of piles in driven chalk. *Engineering in Chalk, Proc Chalk 2018 Conf*, pp. 33-51. London, UK: ICE Publishing. 10.1680/eiccf.64072.033

Lehane B.M. & White D.J. (2005) Lateral stress changes and shaft friction for model displacement piles in sand. *Can Geotech J,* 42 (4), 1039-1052. 10.1139/T05-023

Leroueil S. & Vaughan P.R. (1990) The general and congruent effects of structure in natural soils and weak rocks. *Géotechnique,* 40 (3), 467-488. 10.1680/geot.1990.40.3.467

Lord J.A., Clayton C.R.I. & Mortimore R.N. (2002) *CIRIA Report C 574: Engineering in Chalk*, London, UK: Construction Industry Research and Information Association (CIRIA).

Lord J.A., Twine D.P. & Yeow H. (1994) *CIRIA Project Report 11: Foundations in chalk*, London, UK: Construction Industry Research and Information Association (CIRIA).

Madhusudhan B.N. & Baudet B.A. (2014) Influence of reconstitution method on the behaviour of completely decomposed granite. *Géotechnique,* 64 (7), 540-550. 10.1680/geot.13.P.159

Matthews M.C. & Clayton C.R.I. (1993) Influence of the intact porosity on the engineering properties of a weak rock. *Proc Int Symp Geotech Engr Hard Soils - Soft Rocks* (1), pp. 693-702. Rotterdam, NL: A. A. Balkema.

Paganin D., Mayo S.C., Gureyev T.E., Miller P.R. & Wilkins S.W. (2002) Simultaneous phase and amplitude extraction from a single defocused image of a homogeneous object. *J Microsc,* 206 (1), 33-40. 10.1046/j.1365-2818.2002.01010.x

Ramachandran G.N. & Lakshminarayanan A.V. (1971) Three-dimensional reconstruction from radiographs and electron micrographs: application of convolutions instead of Fourier transforms. *PNAS,* 68 (9), 2236-2240. 10.1073/pnas.68.9.2236

Rowe P.W. (1962) The stress-dilatancy relation for static equilibrium of an assembly of particles in contact. *Proc R Soc Lond A,* 269 (1339), 500-527. 10.1098/rspa.1962.0193

Schnaid F. & Mántaras F.M. (2003) Cavity expansion in cemented materials: structure degradation effects. *Géotechnique,* 53 (9), 797-807. 10.1680/geot.2003.53.9.797

van Aarle W., Palenstijn W.J., Cant J., Janssens E., Bleichrodt F., Dabravolski A., et al. (2016) Fast and flexible X-ray tomography using the ASTRA toolbox. *Opt Express,* 24 (22), 25129-25147. 10.1364/OE.24.025129

Vo N.T., Atwood R.C. & Drakopoulos M. (2018) Superior techniques for eliminating ring artifacts in X-ray micro-tomography. *Opt Express,* 26 (22), 28396-28412. 10.1364/OE.26.028396

Wadeson N. & Basham M. (2016) Savu: A Python-based, MPI Framework for Simultaneous Processing of Multiple, N-dimensional, Large Tomography Datasets. arXiv:1610.08015 [Preprint]